

X-ray Diffraction Study and Texture Evolution for a Ti-Nb-Ta Biomedical Alloy Processed by Accumulative Roll Bonding

Anna Nocivin, Doina Raducanu, Ion Cinca, Corneliu Trisca-Rusu, Mihai Butu, Isabelle Thibon, and Vasile Danut Cojocaru

(Submitted July 9, 2014; in revised form January 22, 2015; published online February 18, 2015)

A Ti-25Nb-25Ta β -type alloy was subjected to severe plastic deformation via accumulative roll bonding; the method was applied on two different precursor samples, in order to establish the influence of the precursor structural state on the final alloy properties processed by ARB. \overline{Bo} and \overline{Md} electronic parameters have been calculated in order to establish, by plotting the alloy on \overline{Bo} - \overline{Md} diagram, the alloy β stabilizing grade, and the dominant deformation mechanisms. Structural modifications during ARB process (changes in phase structure, phase quantities, lattice parameters, and coherent crystalline domain size) were described and analyzed using XRD investigations. Texture data expressed by pole figures, inverse pole figures, and orientation distribution functions for the (110), (200), and (211) β -Ti peaks were obtained through XRD investigations. The results showed that it is possible to obtain high intensity share texture modes $\{001\}\langle 110 \rangle$ and well-developed α - and γ -fibers, the most important fiber being the α -fiber.

Keywords β -Ti alloy, ARB processing, \overline{Bo} - \overline{Md} electronic parameters, texture, XRD

1. Introduction

An intense research work for developing highly biocompatible Ti-based alloys for medical applications has been performed in the last years (Ref 1-8).

Development of metastable β -Ti alloys is a goal motivated by some exquisite qualities: superior biocompatibility and corrosion resistance, high strength to density ratio, high mechanical resistance and low elastic modulus value, closer to natural bone (Ref 6, 7, 9-15). Ti alloys containing only β phase are easier to be mechanical processed (compared to alloys containing HC- α phase) and therefore, grain refining is possible until the structures reach ultra-fine or nano-crystalline (NC) level. It is considered (Ref 3-7) that nano-structured Ti alloys exhibit appealing structural characteristics which can improve properties such as bioactivity and mechanical performance (high strength, high toughness, or super-elasticity at ambient temperatures); they exhibit superior qualities compared with their coarse-grained counterparts. Consequently, the present work is focused on ultra-fine grained (UFG) or NC structures induced by severe plastic

deformation (SPD) on a recently new developed β -type alloy: Ti-25Nb-25Ta. From several SPD methods, accumulative roll bonding (ARB) has been selected (Ref 16-19). It involves SPD of metallic sheets, without modification of overall material thickness. In real terms, ARB consists in plastic deformation by rolling of two equally geometrical dimensioned stacked material sheets, with a deformation degree of 50%. In these conditions, the final consolidated stacked sheet will have a final thickness equal to that of each original sheet before rolling. The ARB process can be applied on bulk materials and has a major advantage consisting in unlimited plastic deformation for an unlimited number of ARB cycles (Ref 16-19). Through this method, the grain dimensions decrease after each ARB cycle, until UFG or even NC structure level is obtained.

The aim of the present study is to explore the Ti-25Nb-25Ta alloy characteristics (targeted to texture evolution) in UFG/NC structural state, obtained by applying an ARB process, starting from two different alloy structural states as precursor.

It is to be mentioned that Ti-25Nb-25Ta alloy has suitable properties for biomedical applications, proved by microstructural, chemical, and mechanical investigations, carried out in several recent published studies (Ref 19-24) but pertaining only to equiaxed homogeneous grain microstructure and not to UFG/NC structural state.

2. Material and Methods

2.1 Alloy Synthesis, Thermo-Mechanical Processing, and ARB Processing

The alloy composition Ti-25Nb-25Ta (wt.%) was obtained from commercially pure elements, using a levitation induction melting furnace FIVE CELES—MP25 with a nominal power of 25 kW and a melting capacity of 30 cm³, under argon protective atmosphere. The obtained chemical composition had no more than 0.1 wt.% compositional variations compared

Anna Nocivin, Faculty of Mechanical, Industrial and Maritime Engineering, Ovidius University of Constanta, 900527 Constanta, Romania; **Doina Raducanu**, **Ion Cinca**, and **Mihai Butu**, Faculty of Materials Science and Engineering, POLITEHNICA University of Bucharest, 313 Spl. Independentei, 060042 Bucharest, Romania; **Corneliu Trisca-Rusu**, National Institute for Research and Development in Microtechnologies, 126A Erou Iancu Nicolae Street, 077190 Bucharest, Romania; and **Isabelle Thibon**, INSA Rennes, UMR CNRS 6226 SCR / Chimie-Métallurgie, 35708 Rennes Cedex, France. Contact e-mails: anocivin@univ-ovidius.ro and doina.raducanu@mdef.pub.ro.

with the initial proposed one, being considered negligible. It must be emphasized that this technological alloy synthesis method is efficient for melting metals with a big difference between their melting temperatures; ingots with high chemical homogeneity, without risk of contamination, are obtained. For the present case, the large difference in melting temperatures (Ti = 1660 °C; Ta = 2996 °C; Nb = 2468 °C) required the re-melting of the obtained ingots twice, in order to obtain a high degree of chemical homogeneity.

Ti-25Nb-25Ta alloy has been further thermo-mechanically processed (TM) in order to obtain thin precursor strips needed to apply further ARB (Fig. 1). Multi-layered stacked strips, consisting of 8 layers stacks, were finally obtained.

The TM process started with cold rolling (CR I) with a relative deformation degree of about 84.32% (equivalent strain $\epsilon = 1.85$) realized by 20 rolling passes, followed by a recrystallization treatment in argon protective atmosphere, at 850 °C/30 min/air cooling, using a GERO SR 100 × 500 heat treatment oven. The recrystallization treatment was performed in order to remove the strain-hardening effects after first cold-rolling stage. TM continued with a second cold-rolling (CR II) stage with a relative deformation degree of about 71.05% (equivalent strain $\epsilon = 1.24$) realized by 16 rolling passes; the final strip thickness was 141 μm . The strips obtained by the procedure described above represent the so called precursor-1. The experiments continued with a part of precursor-1 samples. They were subjected to a final recrystallization treatment (in same conditions like previous recrystallization treatment) in order to obtain the so called precursor-2.

Both precursors were distinctly ARB processed, in the same conditions. Before ARB process, all samples were cleaned

using an ultrasonic bath at 60 °C, in ethylic alcohol. The ARB process consisted in three passes in order to obtain 2 layers (after first ARB pass), 4 layers (after second ARB pass), and 8 layers (after third ARB pass) stacks. Cold-rolling processes (CR I and CR II) and ARB passes were performed using a Mario di Maio LQR120AS rolling mill, at 3 m/min rolling speed, without any lubrication.

2.2 Alloy Structural Characterization

2.2.1 X-ray Diffraction. The phase structure and phase characteristics evolution, during the experimental program, were studied on the as-cast alloy, precursor-1, precursor-2, and on the final ARB-processed specimens (with 8 layers stacks) by XRD methods, using a Panalytical X'Pert PRO MRD diffractometer, with Cu k-alpha ($\lambda = 0.15418 \text{ nm}$) in the range $2\theta = 30^\circ$ to 80° and with a step size of 0.02, 40 kV, and 30 mA. The x-ray diffraction patterns were recorded on the RD and TD plane surfaces of the ARB-processed sheets. The recorded XRD spectra were fitted using PeakFit v4.11 software package, in order to determine for each diffraction peak: the position, the intensity, and peak broadening—full width at half maximum (FWHM) parameters.

2.2.2 Rolling Texture Characterization. Texture features in precursors and ARB-processed specimens (with 8 layers stacks) were analyzed using (110), (200), and (211) β -Ti pole figures obtained using a Philips PW 3710 diffractometer, with Cu k-alpha ($\lambda = 1.5418 \text{ \AA}$) wavelength. The pole figure raw data were fitted and analyzed using MTEX v3.2.2 open source software package (Ref 25, 26), in order to calculate inverse pole figures (IPFs) and orientation distribution functions (ODFs).

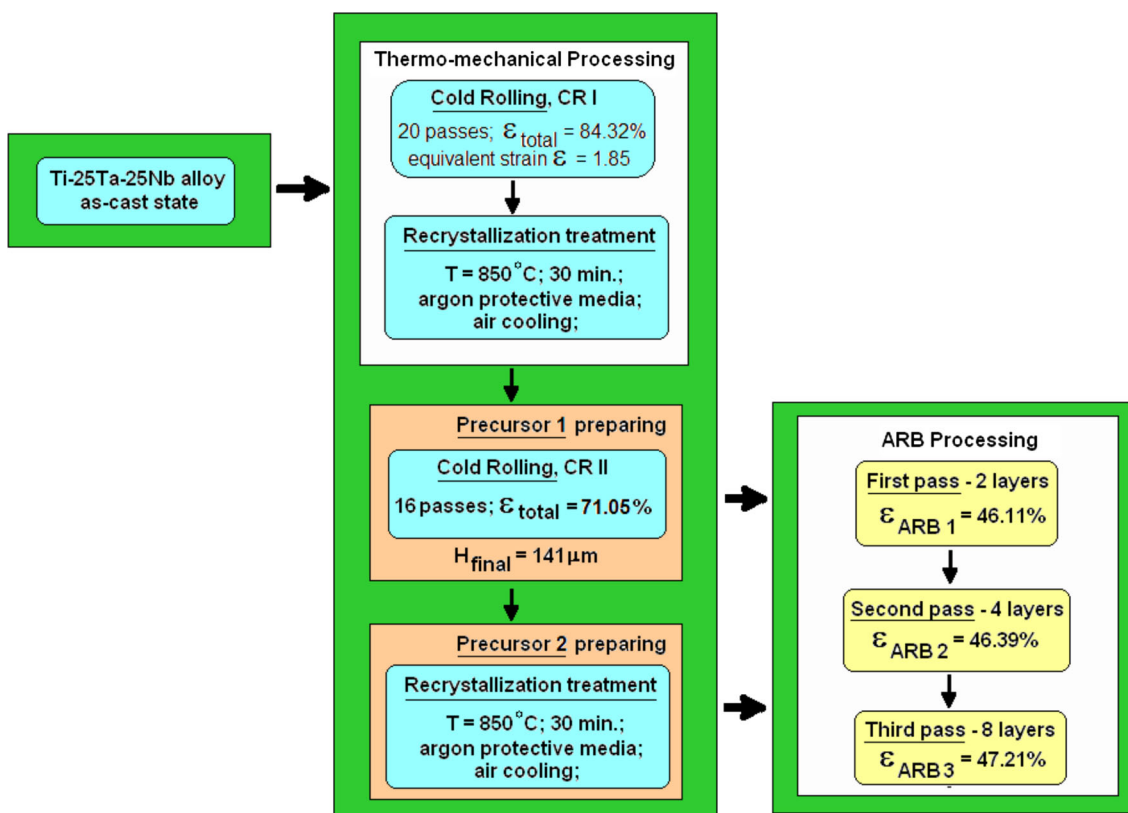


Fig. 1 Experimental program applied to Ti-25Nb-25Ta alloy

2.2.3 TEM-EDS Analysis. Structural investigations concerning obtained nanostructure in the case of resulted ARB strips with 8 layers were performed using a TECNAI G2 F30 S-Twin HRTEM.

3. Results and Discussions

3.1 Theoretical Analysis of the β -Phase Stability Using \overline{Bo} - \overline{Md} Diagram

The grain refining of β -Ti-based alloys during SPD depends on structural deformation mechanisms acting by dislocations slip or twinning of β phase, and/or stress-induced martensitic transformation; the dominant mechanism basically depends on β phase stability (Ref 3-7); in these conditions, it is important to analyze alloy β stabilizing grade in order to anticipate the deformation behavior during the SPD/ARB process. The β -phase stability in Ti-based alloys increases with rising content of the β -stabilizing elements such as Mo [the strongest β stabilizing element (Ref 27)], Nb, Ta, or Zr. The $[Mo]_{eq}$ is commonly used to evaluate the β phase stability (Ref 28):

$$\begin{aligned} \%[Mo]_{eq} = & 1.00(\%Mo) + 0.28(\%Nb) + 0.22(\%Ta) \\ & + 0.67(\%V) + 1.6(\%Cr) + 2.9(\%Fe) \quad (\text{Eq 1}) \\ & - 1.00(\%Al). \end{aligned}$$

Typically, an $[Mo]_{eq}$ of greater than 10 wt.% is regarded as sufficient to preserve the β phase on quenching from above the β -transus (Ref 29).

For the studied alloy, by applying the relation (1), the resulted $[Mo]_{eq}$ is 12.5% of value which indicates high β phase stability. However, in recent years, the attention has been focused on analyzing the β phase stability through electronic parameters describing the bonding characteristics of the β phase, namely the bond order (\overline{Bo}) and d-orbital energy (\overline{Md}) (Ref 30, 31). The \overline{Bo} parameter represents the bond order, which is a measure of the covalent bond strength between Ti and used alloying element. On the other hand, the \overline{Md} parameter represents the d-orbital energy level of an alloying transition metal, which is well correlated with the electronegativity and the metal radius of the element. The average values of \overline{Bo} and \overline{Md} for a certain alloy are defined by taking the compositional average of each parameter. Since the calculations have recently been extended over a variety of alloying elements, \overline{Bo} and \overline{Md} parameters have been calculated for present alloy using data for each alloying component used from (Ref 30) marked with *) in Table 1.

\overline{Bo} - \overline{Md} diagrams have been developed from experimental data in order to predict the effects of alloy composition on

deformation behavior for superior β stable alloys (Ref 6, 30-32). The calculated parameters, $\overline{Bo} = 2.88$ and $\overline{Md} = 2.45$, have been used for plotting the as-studied alloy on \overline{Bo} - \overline{Md} diagram (Fig. 2).

In Fig. 2, the boundaries $\beta/\beta+\alpha''/\omega$ and $\beta+\alpha''/\omega/\beta$, together with the boundaries for M_s = room temperature (RT) and M_f = RT, are indicated. Also, the domains referring to dominant deformation structural mechanisms that occur during cold deformation of the alloy (by slip of dislocations, by twinning of β phase or by stress-induced martensitic transformation) are illustrated. With decreasing stability, reflected by \overline{Md} increase or the \overline{Bo} decrease, the deformation mechanism changes from dislocation slip to twinning and/or martensitic transformation (Ref 30); it is a general correlation between the phase stability and β Ti alloys deformation mechanisms by demarcation of a border line between single β domain and $\beta+\alpha''/\omega$ domain in \overline{Bo} - \overline{Md} diagram.

The M_s —the starting temperature of martensitic transformation—can be calculated using the formula from (Ref 33). This formula has been determined with special reference to β -Ti alloys. Thus, for the as-studied alloy, the calculated M_s [K] = 1156 to 17.6 Nb %gr. = 716 K = 443 °C.

The position of the as-studied alloy in \overline{Bo} - \overline{Md} diagram corresponds to the border of $\beta/\beta+\alpha''/\omega$ phases which indicate that even if $[Mo]_{eq}$ and the amount of β stabilizing elements (Nb and Ta) are high, there is possible that in certain thermo-mechanical conditions, a small amount of α'' precipitates form. Having in view also that the alloy has the M_s , above room temperature, and M_f , below, it can be anticipated that the structure can be formed by β phase and a very small amount of

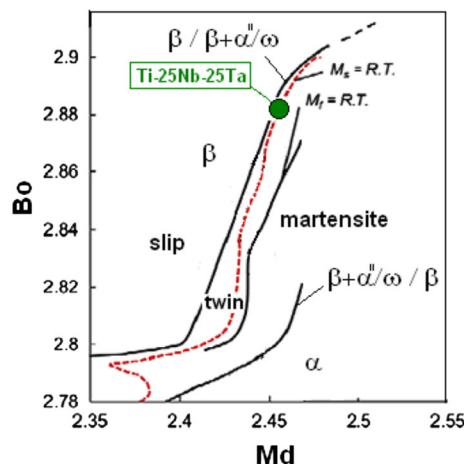


Fig. 2 Extended \overline{Bo} - \overline{Md} diagram from (Ref 30); Ti-25Nb-25Ta alloy position is marked

Table 1 Chemical parameters and \overline{Bo} and \overline{Md} electronic parameters for Ti-25Nb-25Ta alloy [* data from (Ref 30)]

Parameters	Ti	Nb	Ta	Ti-Nb-Ta alloy
Wt.%	50	25	25	
At.%	72	18.5	9.5	
Electro-negativity	1.5	1.6	1.5	
Atomic mass, g/mol	47.90	92.906	180.948	
Valence	2	3	3	
\overline{Bo}	2.79*	3.099*	3.144*	$\overline{Bo} = 2.877$
\overline{Md}	2.447*	2.424*	2.531*	$\overline{Md} = 2.450$

α'' martensite precipitates. However, the alloy position on the diagram cannot conclude a dominant deformation mechanism because of the approached borders between slip, twinning, and stress-induced martensitic transformation domains. Apparently, it can develop all three mechanisms.

These considerations will be useful for hereinafter analyzing the XRD experimental data and also the texture evolution of the studied alloy from the ARB process perspective.

3.2 XRD Analysis

The aim of present study is to show the evolution of Ti-25Nb-25Ta alloy structural features with the progress of experimental program targeted to alloy processing by SPD/ARB. There will be analyzed the as-cast, precursor, and final ARB (three passes/8 layers)-processed samples.

Structural modifications (changes in phase structure, phase quantities, lattice parameters, and coherent crystalline domain size) after ARB process were described and analyzed using XRD investigations, correlated with β -phase stability analysis (presented at section 3.1).

XRD tests have been performed on initial as-cast alloy (Fig. 3) as starting point for comparing the structure evolution during experimental program, *precursor-1* (Fig. 4), *precursor-2* (Fig. 5), ARB-8 layers/ applied on precursor-1, further called *ARB-8 layers-1* (Fig. 6) and ARB-8 layers/applied on precursor-2, further called *ARB-8 layers-2* (Fig. 7).

For the initial as-cast alloy, all structural parameters, deductible from XRD spectra (Fig. 3), are indicated in Table 2. The present study proposes the analysis of the structural characteristics of the precursors compared with ARB-processed samples; all data are included in Table 2 in order to indicate structural features evolution.

The presence of β -Ti and α'' -Ti phases can be observed in variable quantities in all processed structural states. Table 2 indicates the lattice parameters (determined for each crystalline system of the present phases), the phase quantities, the inter-atomic distance (d) corresponding to (hkl) crystallographic planes, and the average of coherent crystalline domain size (D) for both, β -Ti and α'' -Ti phases [calculated using simple Scherer equation (Ref 34)], taking into account the specific phase diffraction lines—fitted position, intensity, and peak broadening.

As dominant phase, the β -Ti phase was identified clearly on the XRD profiles (indexed in bcc system— $Im\bar{3}m$, with diffraction spectra peaks obtained on (110), (200), and (211)

planes) alongside with a minor quantity of α'' -Ti phase (indexed in orthorhombic system— $Cmcm$, with diffraction spectra peaks obtained on (002), (200), and (202) planes).

Using XRD spectra for precursor-1 (Fig. 4), the lattice parameter of β -Ti phase ($a = 0.3284$ nm) and the lattice parameters of α'' -Ti phase ($a = 0.3211$ nm; $b = 0.4731$ nm and $c = 0.4632$ nm) have been determined—all indicated in Table 2. Identical observations were reported in the case of Ti-22Nb-6Ta alloy (Ref 35); the parent β -Ti phase showed similar lattice parameter ($a = 0.3289$ nm) and also α'' -Ti phase ($a = 0.3221$ nm; $b = 0.4766$ nm and $c = 0.4631$ nm). The inter-atomic distance corresponding to (hkl) crystallographic planes, using the obtained diffraction spectra peaks, was also determined (Table 2).

Based on β -Ti (200) and on α'' -Ti (200) diffraction lines, the average of coherent crystalline domain size was determined (28 nm and 31 nm, respectively, Table 2), for both β -Ti and α'' -Ti phases. For precursor-1, the structure is formed by dominant β phase (93.79%) due to β stabilizing alloying elements—Nb and Ta. The XRD spectra also indicate a small quantity of α'' -Ti phase (6.21%—higher, when compared with the as-cast sample), due to cold-rolling process, which favor the development of stress-induced phase transformation, from bcc metastable β phase to orthorhombic α'' -martensite ($\beta \rightarrow \alpha''$). The ability of metastable β -Ti alloys to undergo a deformation—induced martensitic transformation during cold rolling has already been demonstrated (Ref 10, 11, 23, 36). Therefore, the small amount of α'' -Ti phase from precursor samples began to increase step by step during ARB process.

It must be mentioned that XRD-analyzed patterns have not revealed any phase transformation between the β phase and the ω phase during ARB processing, as mentioned in the paper (Ref 40) for the Ti-36Nb-2.2Ta-3.7Zr-0.3O alloy (with less Ta, but additional Zr and O), processed by high-pressure torsion method of SPD. In conformity with (Ref 30), the β phase becomes more stable with increasing content of Ta (from 5 to 20%) and Nb (from 20 to 40%), and the formation of the ω phase is suppressed in these kinds of alloys. Therefore, for the studied alloy, with 25% Ta and 25% Nb, the formation of the ω phase is suppressed, fact argued by XRD images.

Hereinafter, from XRD spectra of precursor-2 analysis (Fig. 5), following observations are to be mentioned: the lattice parameters (a_β for β -Ti phase and $a_{\alpha''}$, $b_{\alpha''}$, $c_{\alpha''}$ for α'' -Ti phase) and inter-atomic distance (d) corresponding to different (hkl) crystallographic planes are similar to precursor-1; however,

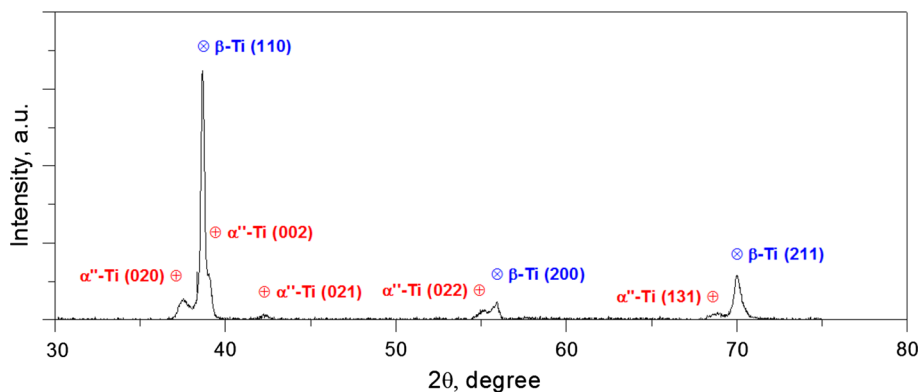


Fig. 3 XRD pattern of the as-cast Ti-25Nb-25Ta alloy

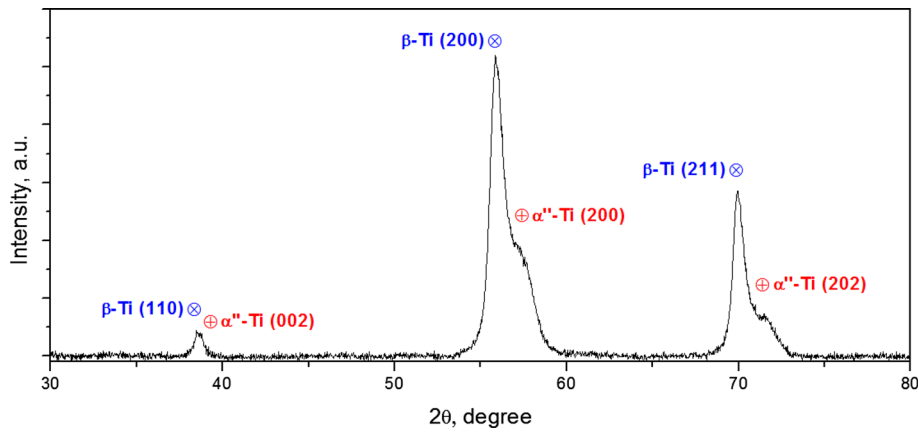


Fig. 4 XRD pattern of Ti-25Nb-25Ta alloy in the state corresponding to precursor-1

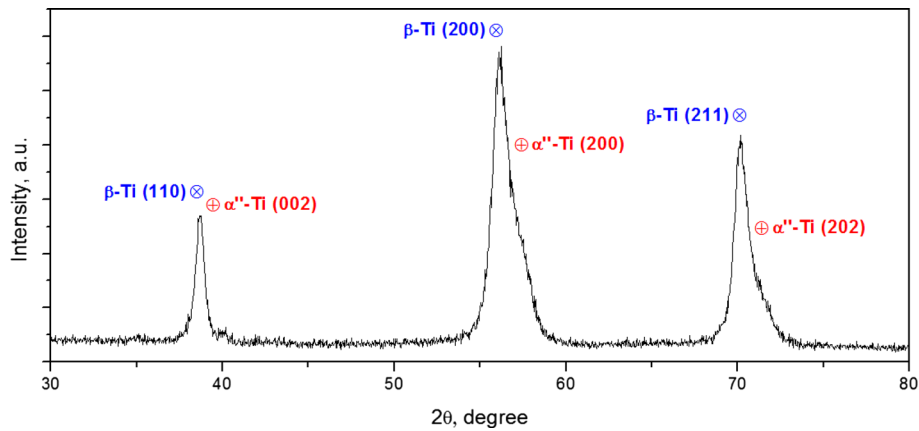


Fig. 5 XRD pattern of Ti-25Nb-25Ta alloy in the state corresponding to precursor-2

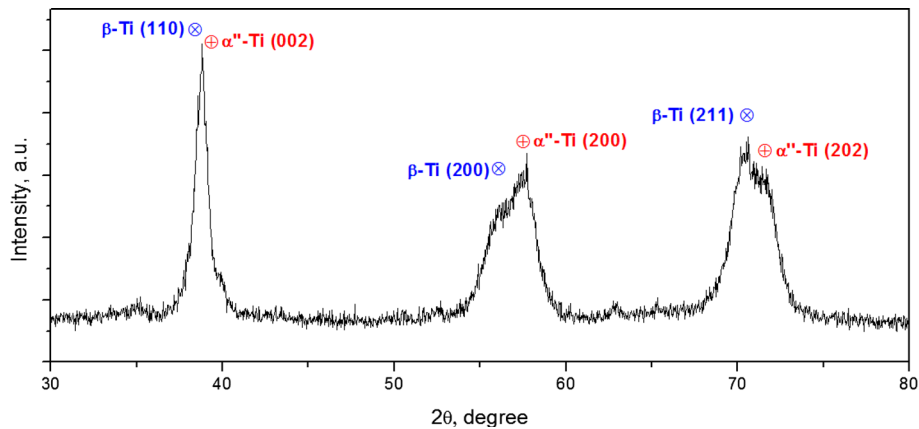


Fig. 6 XRD pattern of Ti-25Nb-25Ta alloy in the state corresponding to ARB-8 layers-1

comparatively with precursor-1, some structural modifications can be observed, due to recrystallization treatment which has been applied on precursor-2: for the β -Ti phase, a greater value for crystalline domain size D (42 nm); instead, a α'' -Ti phase quantity diminution (from 6.2 to 0.38%) was attested by almost insignificant diffraction peaks comparatively with β -Ti phase sharp and high diffraction peaks (Fig. 5) and a four times smaller crystalline domain size D (8 nm). All these phenomena are a consequence of the applied recrystallization treatment, by

which β -Ti phase forms larger recrystallized grains (as usual after this kind of treatment), while α'' -Ti phase becomes reduced and downsized because it dissolves almost entirely in β -Ti phase.

After ARB process applied on precursor-1, the XRD spectra for ARB-8 layers-1 reveal a modified phase quantity of the β -phase and α'' -phase: α'' -Ti phase has quantitatively increased with 33% (from 6.2 to 39.2%) due to main structural phenomenon which occurs during cold deformation—stress-induced martensitic

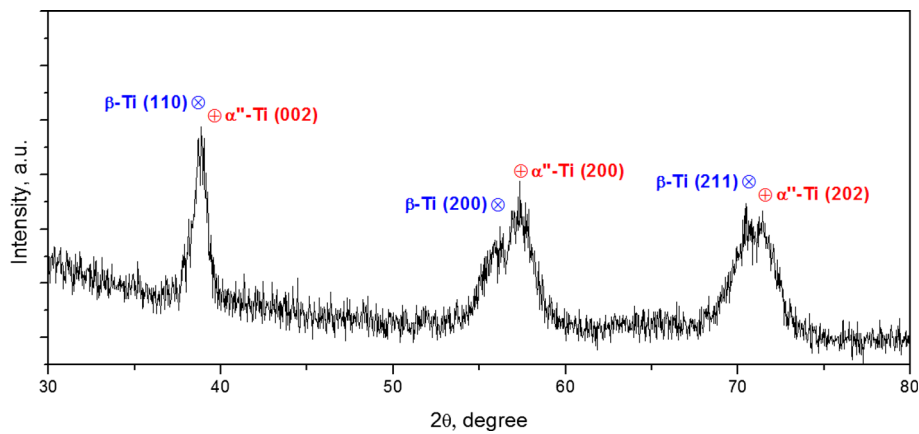


Fig. 7 XRD pattern of Ti-25Nb-25Ta alloy in the state corresponding to ARB-8 layers-2

Table 2 Structural characteristics for Ti-25Nb-25Ta alloy

Structural state of the alloy	Phase content	Lattice parameters	<i>d</i> , nm	<i>D</i> , nm
As-cast	β-Ti phase quantity: 99.52 ± 0.23%	<i>a</i> = 0.3288 nm		82
	α''-Ti phase quantity: 0.48 ± 0.11%	BCC system— <i>Im-3m</i> <i>a</i> = 0.31811 nm; <i>b</i> = 0.4813 nm; <i>c</i> = 0.4631 nm;		14
precursor-1	β-Ti phase quantity: 93.79 ± 1.17%	Orthorhombic system— <i>Cmcm</i> <i>a</i> = 0.3284 nm	0.2321 for (110) plane	28
	α''-Ti phase quantity: 6.21 ± 0.68%	BCC system— <i>Im-3m</i> <i>a</i> = 0.3211 nm; <i>b</i> = 0.4731 nm; <i>c</i> = 0.4632 nm;	0.1641 for (200) plane 0.1340 for (211) plane 0.2271 for (002) plane 0.1608 for (200) plane 0.1319 for (202) plane	31
precursor-2	β-Ti phase quantity: 99.62 ± 0.23%	Orthorhombic system— <i>Cmcm</i> Similar	Similar	42
	α''-Ti phase quantity: 0.38 ± 0.11%			8
ARB-8 layers-1	β-Ti phase quantity: 60.76 ± 1.09%	Similar	Similar	24
	α''-Ti phase quantity: 39.24 ± 0.64%			7
ARB-8 layers-2	β-Ti phase quantity: 58.94 ± 0.84%	Similar	Similar	34
	α''-Ti phase quantity: 41.06 ± 0.36%			5

transformation. The crystalline size of new formed α''-phase is of nano-metric dimensions—about 7 nm.

Concerning the ARB process applied on precursor-2, the XRD spectra for ARB-8 layers-2 reveal also an increased quantity of α''-phase, with about 40.7% (from 0.38 to 41.06%).

For both cases, by ARB applying on two different precursors, the main conclusions are the increasing α'' phase quantity with about 33 to 40% due to stress-induced martensitic transformation. It seems that the recrystallization treatment (which differentiates the two precursors states) favors stress-induced martensitic transformation during ARB, since the higher value of α'' phase quantity (41.06%) is for ARB-8 layers-2.

On the other side, a great-dimensional diminution of α'' phase is observed for ARB applied on precursor-1 (from 31 to 7 nm) comparative to ARB applied on precursor-2 (from 8 to 5 nm). This is just apparently, because 31 nm refers to a very small quantity of α'' phase (6%), formed prior ARB process; during ARB process, a new α'' phase formation takes place, more refined and dominant quantitatively. For ARB applied on precursor-2, there is practically no prior ARB-α'' phase, all 41% percent of α'' phase is newly formed during ARB process by stress-induced martensitic transformation.

As concerning β grain size, by applying ARB on 2 precursors, is not so much dimensional decrease (from 28 to 24 nm and from 42 to 34 nm, respectively) because the main alloy deformation mechanism is represented by stress-induced martensitic transformation which favors α'' phase formation. The slight reduction of the crystalline domain size for the β-phase, of about 14 and 19%, respectively, means that besides the stress-induced martensitic transformation, which apparently represents the main deformation mechanism, a β phase twinning or even a dislocations slip as additional deformation mechanisms can act, as it has been theoretically anticipated in section 3.1.

The cumulated conclusion is as follows: a highly fine NC final structure can be obtained by ARB processing, with variable quantities and crystalline dimensions of β-and α''-phases.

This final NC structure underlines the idea that ARB process is suitable for structure refining to ultra-fine grains correlated with β-Ti/α''-Ti ratio decreasing which can be controlled to obtain the final necessary mechanical properties of the alloy in different ways: if the intention is to obtain a high material strength, it is necessary to steer the structure toward small coherent crystalline domains with a corresponding bigger

α'' -phase quantity; but if the intention is to obtain a low elastic modulus, then a smaller amount of α'' -phase quantity is needed (β -Ti phase exhibits a low elastic modulus, while α'' -Ti phase exhibits a higher elastic modulus). From biomedical point of view, the highly fine NC structure, with additional decrease of the elastic modulus, (Ref 10) represent an important desiderate for bone implant applications.

Taking into account the position of the alloy in the \overline{Bo} - \overline{Md} diagram at the border between two domains—twining of the β -phase and stress-induced martensitic transformation—it is possible, through very fine changes in thermo-mechanical processing parameters to change the type of structural deformation mechanisms, from martensite transformation to twinning,

which means the possibility of alloy mechanical properties changing, from one with high strength due to martensitic transformation, to another one with high elasticity or even super-elasticity due to twining of β phase. These considerations require future and more detailed analysis.

In addition to XRD analysis, it has been also performed a TEM-EDS analysis of the structure evolution during the experimental program in order to correlate the obtained results. Figure 8 indicates the HR-TEM-EDS images of nanostructures for precursor-2 and after applying ARB on precursor-2.

The observed nanostructure reveals a highly refined grain structure. It can be observed that the smallest NC domains have dimensions of 6 to 13 nm for the precursor-2, and 4 to 6 nm for

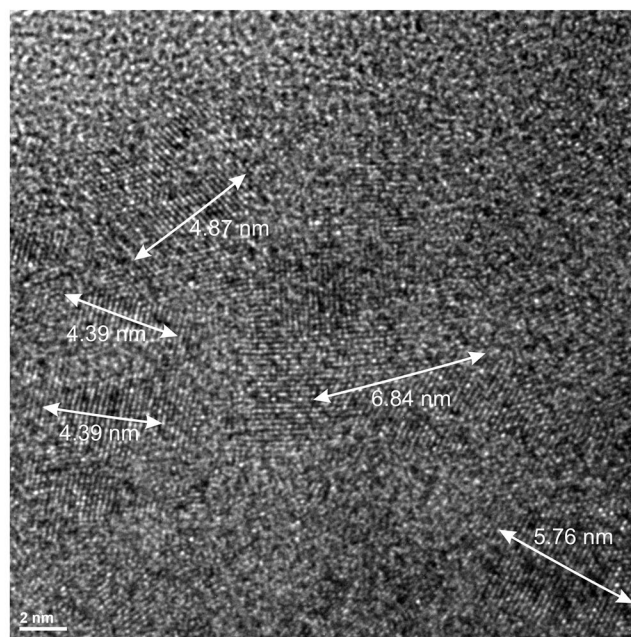
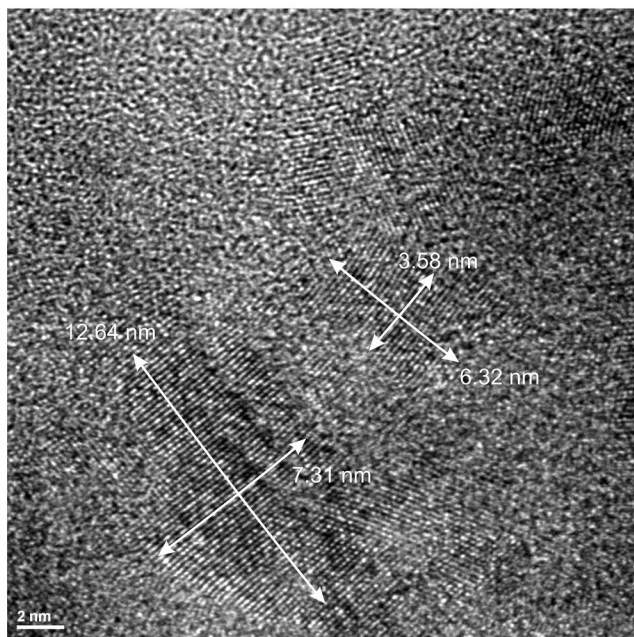
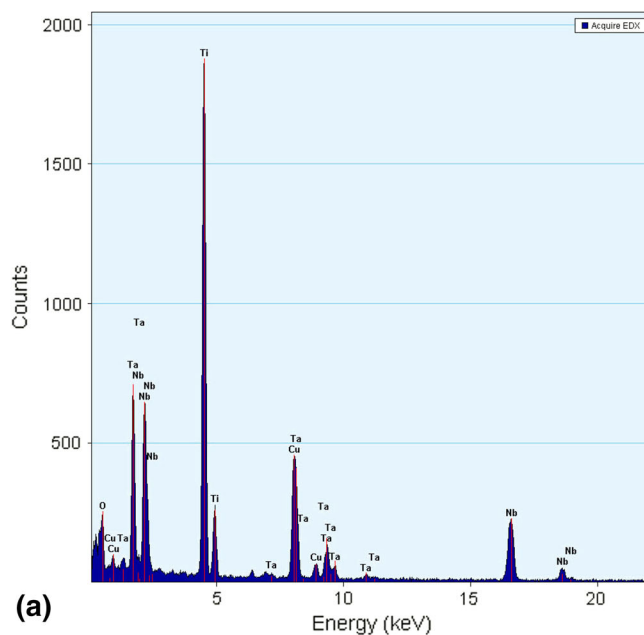


Fig. 8 TEM-EDS images of Ti-25Nb-25Ta alloy: (a) EDS results; (b) precursor-2; and (c) ARB-8 layers-2

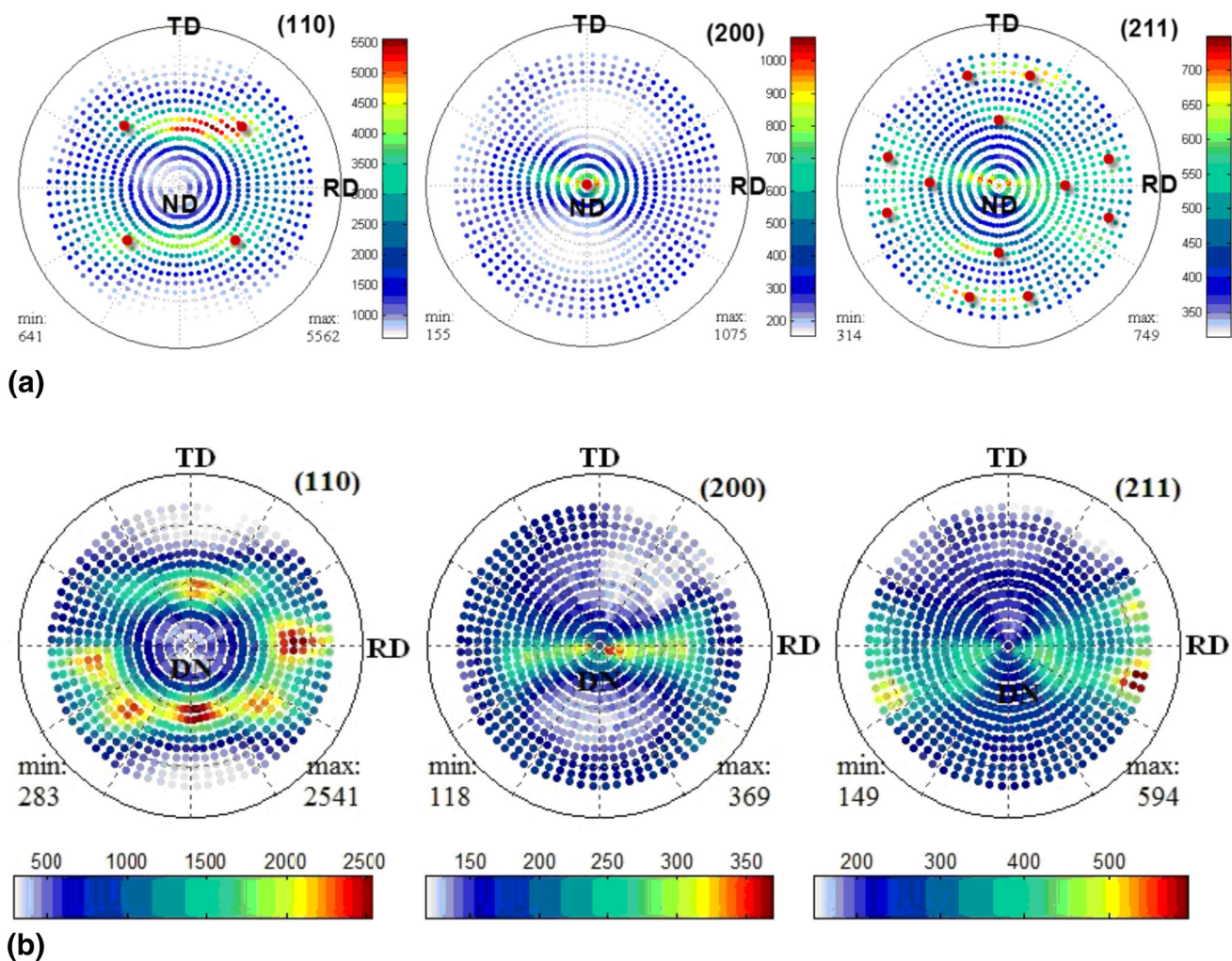


Fig. 9 Images of (110), (200), and (211) raw data pole figure of Ti-25Nb-25Ta alloy for (a) precursor-1; (b) ARB-8 layers-1

ARB-8 layers-2. It has been captured and measured only the smallest NC grains corresponding to α'' -phase (in amount of 0.38% for precursor-2 and 41% for ARB-8 layers-2).

3.3 Analysis of the Rolling Texture

Using (110) raw pole figure data, the IPF's and the ODF's were calculated and plotted. A few assumptions were made: the material crystalline symmetry was indexed in cubic $Im\bar{3}m$ system, while the specimen symmetry in orthorhombic mmm system.

Figure 9 shows collected raw data for (110), (200), and (211) β -Ti pole figures for the precursor-1 (Fig. 9a) and for ARB-8 layers-1 (Fig. 9b). All pole figures were plotted having in view the following directions (sample reference frame): [100]—rolling direction (RD); [010]—transversal direction (TD); and [001]—normal direction (ND).

A well-developed rolling texture is confirmed in precursor-1 specimens (Fig. 9a): the (110) pole figure shows four high intensity peaks symmetrically located around 45° from the center and 45° from both RD and TD. This means that the RD is parallel to [110] crystal direction. The (200) pole figure shows the presence of only one high intensity central peak, while the (211) pole figure shows four symmetrically high intensity peaks located around 28° from the center and 45°

from both RD and TD, and eight symmetrically located peaks around 60° from the center and 15° from RD and TD. In all (110), (200), and (211) pole figures, the identified peaks show distribution characteristics for body-centered cubic (bcc) crystalline structures.

For the ARB-8 layers-1 sample (Fig. 9b), the (110) pole figure shows four high intensity peaks, symmetrically located around 45° from the center and two high intensity peaks located around 60° from the center. The (200) pole figure shows the presence of only one high intensity central peak. As for the (211) figure pole, this one shows two high intensity peaks situated at 60° from the center and at 15° from the RD.

The (110) and (200) pole figures for both, precursor-1 and ARB-8 layers-1, present similar peaks distribution; differences can be observed only in the case of (211) pole figure. These differences may be explained due to stress-induced α'' -Ti phase presence (smaller coherent crystalline size for both parent β -Ti phase and transformed α'' -Ti phase) and β -Ti to α'' -Ti lattice accommodation.

Although pole figure shows how the specified crystallographic directions are distributed in the sample reference frame, the inverse pole figure shows how a selected direction in the sample reference frame is distributed in the reference frame of the crystal. Figure 10 indicates the (110) IPF's for RD, TD, and

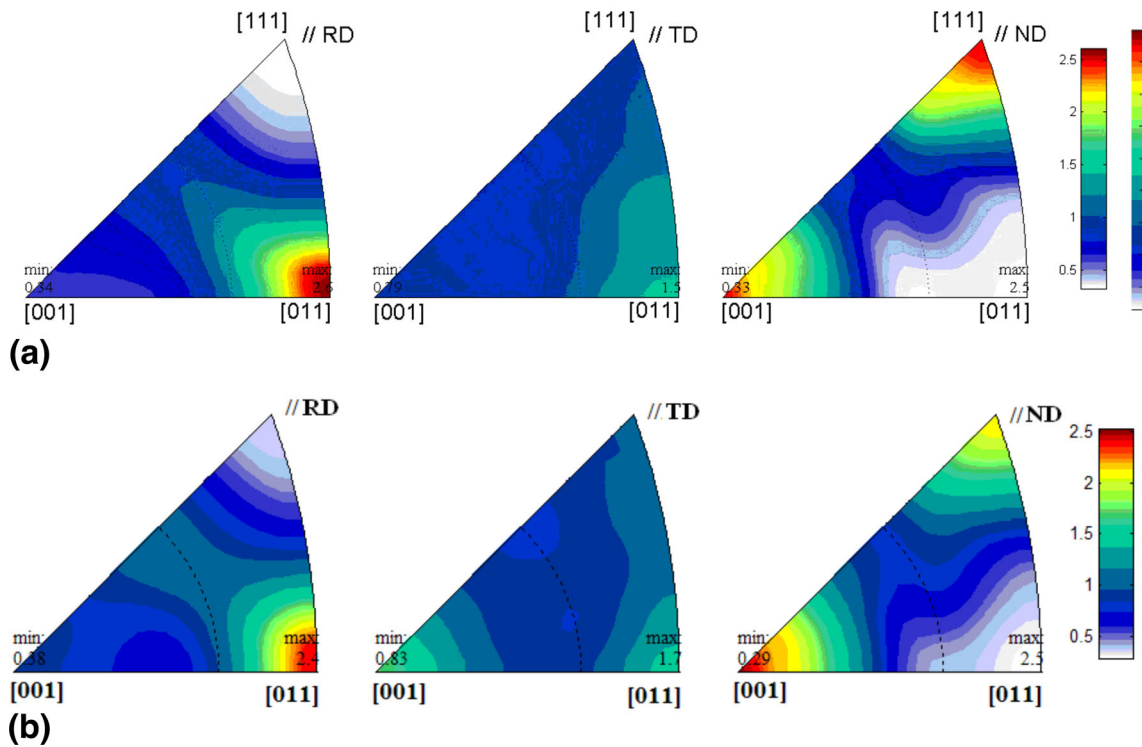


Fig. 10 (110) inverse pole figure for RD, TD, and ND directions for (a) precursor-1; (b) ARB-8 layers-1

ND directions in the case of precursor-1 (Fig. 10a) and ARB-8 layers-1 (Fig. 10b).

For the precursor-1 (Fig. 10a), the inverse pole figure for the RD direction shows what crystallographic directions are most likely parallel to sample rolling direction in the polycrystalline material; for this case, the [011]//RD pair reaches an intensity close to 2.6. For the TD direction, a low intensity pair is formed: [011]//TD with intensity close to 1.5. High intensities are obtained in the case of [001]//ND and [111]//ND pairs, close to 2.5 for both pairs.

For the ARB-8 layers-1 (Fig. 10b), the inverse pole figure indicates that the following high intensity pairs are present: [011]//DL with intensity of 2.4; [011]//DN with intensity of 2.5; and [011]//DT with intensity of 1.7. As a general remark, based on inverse pole figure analysis, the developed texture for ARB 8 layer-processed state shows [001]//ND, [111]//ND, and [011]//RD components.

Since the properties of many important engineering materials are strongly direction dependent, the inverse pole figure is very useful in predicting and calculating the average properties of polycrystalline material along a chosen direction (Ref 37, 38).

The crystallographic textures are typically presented in the reduced Euler space using the Bunge system ($\varphi_1 - \Phi - \varphi_2$) ($\varphi_1 = 0-90^\circ$; $\Phi = 0-90^\circ$; $\varphi_2 = 0-90^\circ$). The most relevant texture fibers developed in bcc metals are (Ref 39)

- α -fiber (crystallographic fiber axis $\langle 110 \rangle$ parallel to RD with major components: $\{001\}\langle 110 \rangle$; $\{112\}\langle 110 \rangle$; $\{111\}\langle 110 \rangle$);
- γ -fiber (crystallographic fiber axis $\langle 111 \rangle$ parallel to ND with major components: $\{110\}\langle 110 \rangle$; $\{111\}\langle 112 \rangle$);
- η -fiber (crystallographic fiber axis $\langle 001 \rangle$ parallel to RD with major components: $\{001\}\langle 100 \rangle$; $\{011\}\langle 100 \rangle$);

- ζ -fiber (crystallographic fiber axis $\langle 011 \rangle$ parallel to ND with major components: $\{011\}\langle 100 \rangle$; $\{011\}\langle 211 \rangle$; $\{011\}\langle 111 \rangle$; $\{011\}\langle 011 \rangle$);
- ε -fiber (crystallographic fiber axis $\langle 011 \rangle$ parallel to TD with major components: $\{001\}\langle 011 \rangle$; $\{112\}\langle 111 \rangle$; $\{111\}\langle 112 \rangle$; $\{011\}\langle 100 \rangle$); and
- θ -fiber (crystallographic fiber axis $\langle 001 \rangle$ parallel to ND with major components: $\{001\}\langle 100 \rangle$; $\{001\}\langle 110 \rangle$).

For bcc metals, the most important ODF sections correspond to rotation angle φ_2 , equal to 0° and 45° .

Figure 11 indicates the calculated ODF sections for precursor-1 state. Plotted ODF section corresponding to $\varphi_2 = 0^\circ$ shows the presence of high intensity texture modes $\{001\}\langle 1\bar{1}0 \rangle$ and $\{010\}\langle 101 \rangle$ with a maximum orientation density of 5.9; both texture modes belong to θ -fiber ($\{001\}\langle 110 \rangle$ family) and are formed due to grains shear during cold-rolling deformation.

The ODF section corresponding to $\varphi_2 = 45^\circ$ shows the presence of the following texture modes and fibers:

- high intensity texture modes $\{001\}\langle 1\bar{1}0 \rangle$ and $\{001\}\langle \bar{1}10 \rangle$, showing a maximum orientation density of 5.9; both texture modes belong to θ -fiber ($\{001\}\langle 110 \rangle$ family) and are formed due to grains shear during cold-rolling deformation;
- well-developed γ -fiber: the main component of γ -fiber stretches from $\{111\}\langle 1\bar{1}0 \rangle$ to $\{111\}\langle \bar{1}\bar{1}2 \rangle$; the γ -fiber is the most important developed fiber during TM processing, with a maximum orientation density of 4; and
- well-developed α -fiber: the main component of α -fiber stretches from $\{001\}\langle 1\bar{1}0 \rangle$ to $\{112\}\langle \bar{1}\bar{1}0 \rangle$; the orientation density of α -fiber shows a value close to 4.6, bigger than the case of γ -fiber.

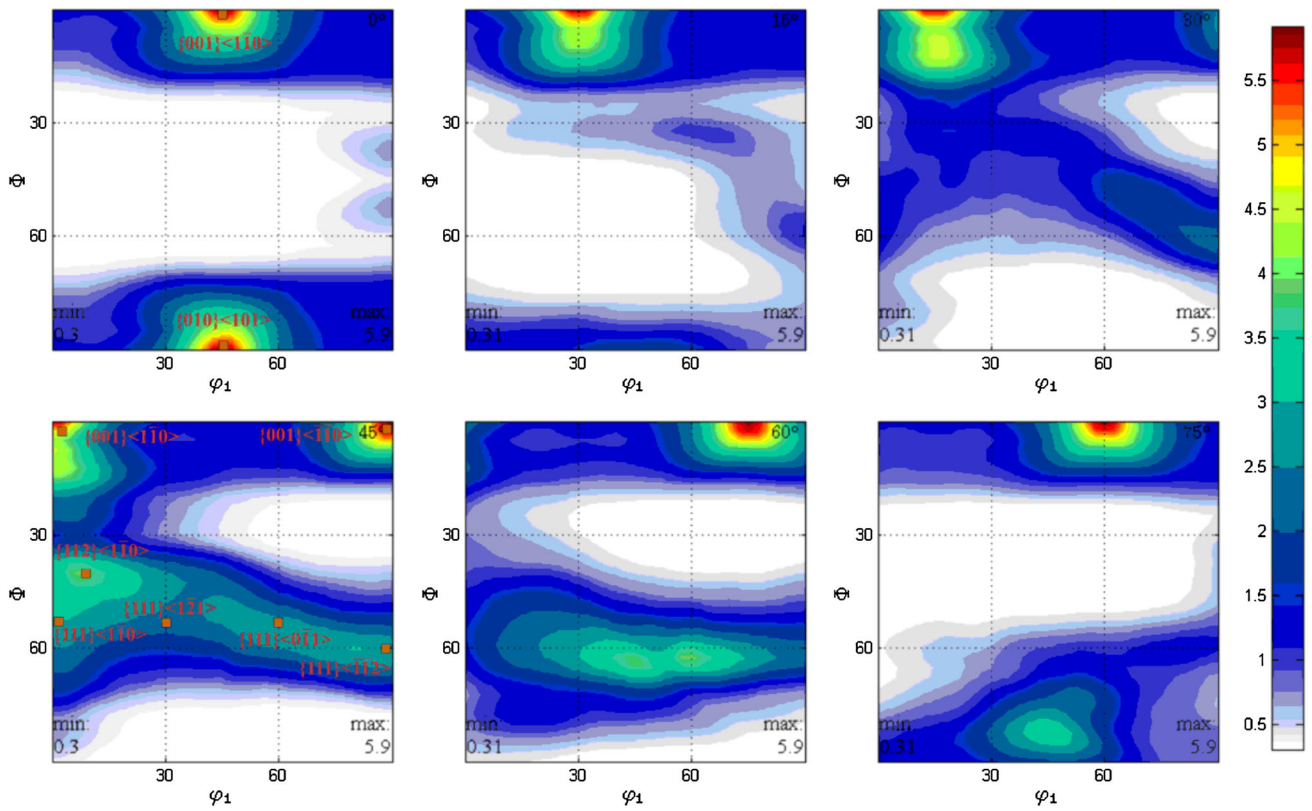


Fig. 11 Orientation distribution function (ODF) for Ti-25Nb-25Ta alloy corresponding to precursor-1 (ODF sections: $\phi_2 = 0^\circ, 15^\circ, 30^\circ, 45^\circ, 60^\circ,$ and 75°)

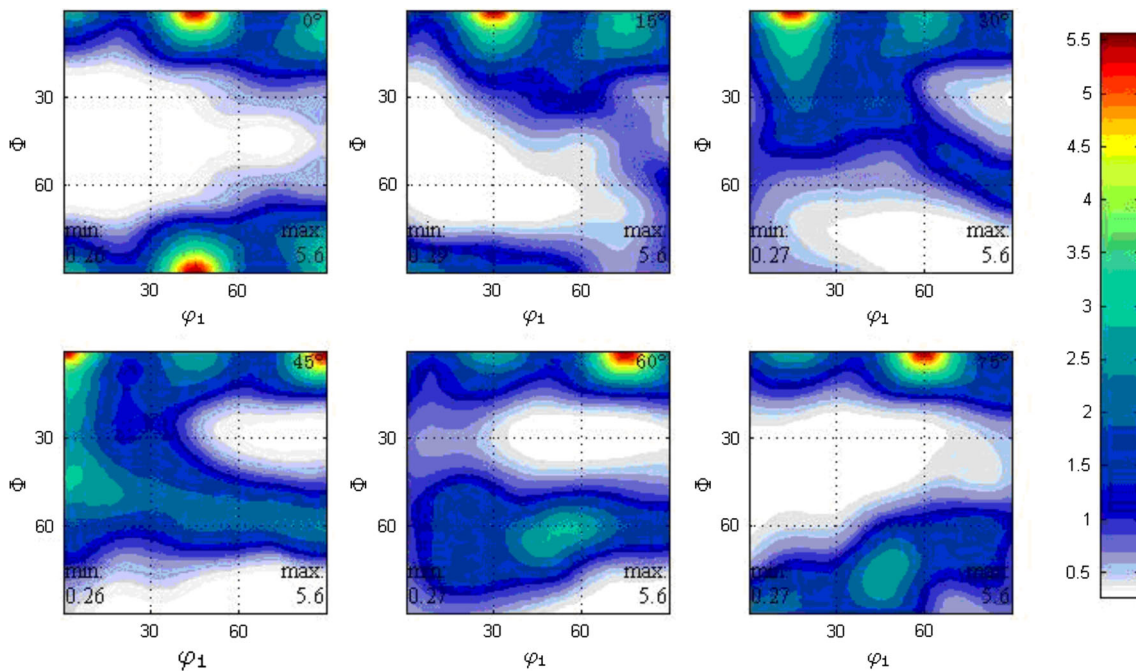


Fig. 12 Orientation distribution function (ODF) for Ti-25Nb-25Ta alloy for ARB-8 layers-1 (ODF sections: $\phi_2 = 0^\circ, 15^\circ, 30^\circ, 45^\circ, 60^\circ,$ and 75°)

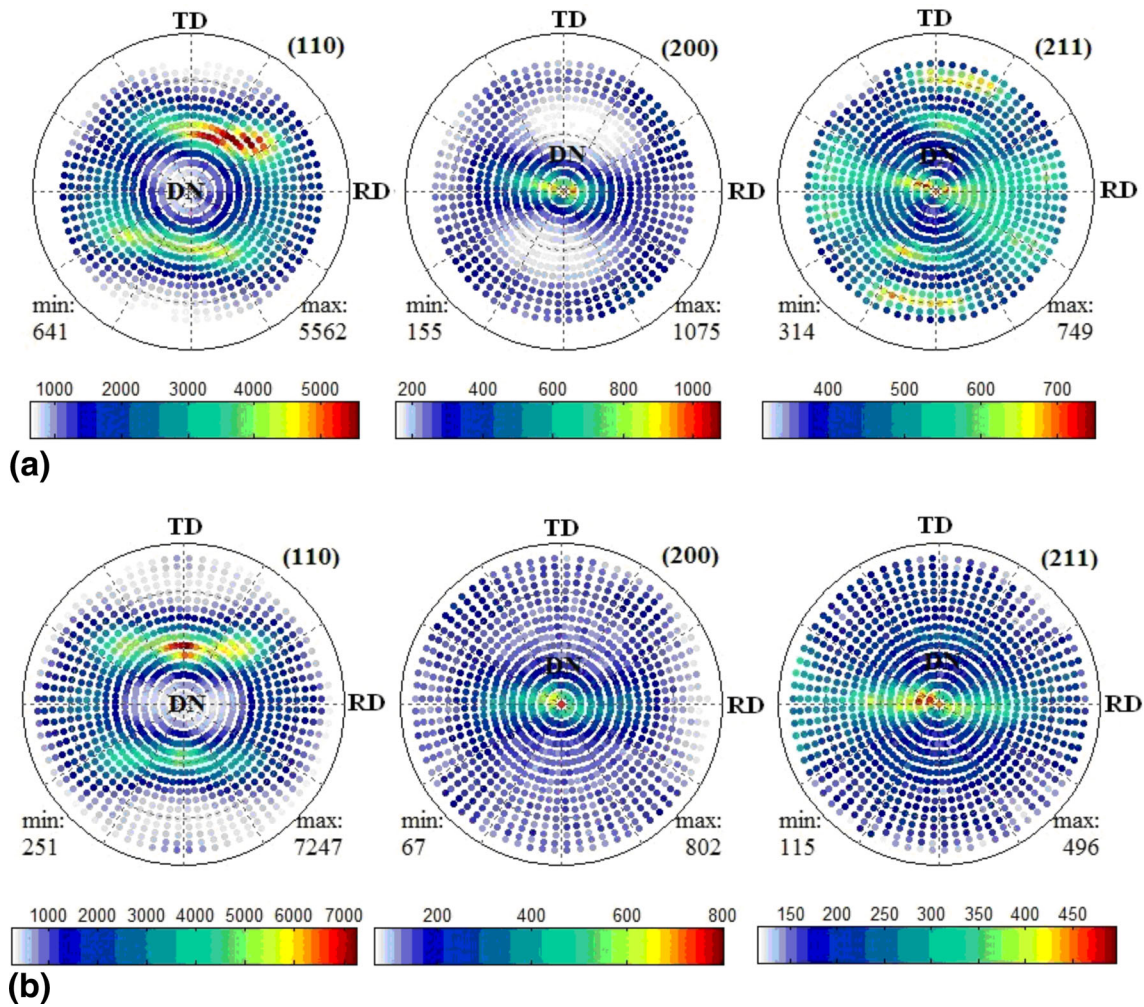


Fig. 13 Images of (110), (200), and (211) raw data pole figure of Ti-25Nb-25Ta alloy for (a) Precursor-2; (b) ARB-8 layers-2

Figure 12 indicates the calculated ODF sections for ARB-8 layers applied on precursor-1. Plotted ODF section corresponding to $\varphi_2 = 0^\circ$ shows the presence of high intensity texture modes $\{001\} \langle 1\bar{1}0 \rangle$ and $\{010\} \langle 101 \rangle$ with a maximum orientation density of 5.6; both texture modes belongs to θ -fiber ($\{001\} \langle 110 \rangle$ family) and are formed due to grains shear during ARB processing.

The ODF section corresponding to $\varphi_2 = 45^\circ$ shows the presence of the following texture modes and fibers:

- high intensity texture modes $\{001\} \langle 1\bar{1}0 \rangle$ and $\{001\} \langle \bar{1}\bar{1}0 \rangle$, showing a maximum orientation density close to 5.6; both texture modes belong to θ -fiber ($\{001\} \langle 110 \rangle$ family) and are formed due to grains shear during ARB processing;
- well-developed γ -fiber: the main component of γ -fiber stretches from $\{111\} \langle 1\bar{1}0 \rangle$ to $\{111\} \langle \bar{1}\bar{1}2 \rangle$; the γ -fiber is the most important developed fiber during ARB processing, with an orientation density close to 5; and
- well-developed α -fiber: the main component of α -fiber stretches from $\{001\} \langle 1\bar{1}0 \rangle$ to $\{112\} \langle 1\bar{1}0 \rangle$; the orientation density of α -fiber shows a value close to 6, bigger than for the γ -fiber case.

Figure 13 shows collected raw data for (110), (200), and (211) β -Ti pole figures in the case of precursor-2 (Fig. 13a) and ARB-8 layers applied on precursor-2 (Fig. 13b). Figure 13a, corresponding to precursor-2, presents the same high intensity peaks distribution like Fig. 9a corresponding to precursor-1, on all three analyzed pole figures: PF (110), (200), and (211). In all pole figures, the identified peaks show specific distributions characteristic for bcc crystalline structures.

Figure 13b corresponds to ARB-8 layers applied on precursor-2. The (110) and (200) pole figures for both, precursor-2 (Fig. 13a) and ARB-8 layers sample (Fig. 13b), present similar peaks distribution, while differences can be observed only in the case of (211) pole figure. These differences may be explained due to stress-induced α'' -Ti phase presence and β -Ti to α'' -Ti lattice accommodation.

Figure 14 illustrates the (110) inverse pole figure for RD, TD, and ND directions in the case of precursor-2 state (Fig. 14a) and ARB-8 layers applied on precursor-2 (Fig. 14b). If the RD of precursor-2 sample is considered, the IPF (Fig. 14a) shows which crystallographic direction from polycrystalline material can be parallel with RD of the sample; in this case, the pair $[011]//RD$ has an intensity of 2.0; in case of TD, a pair $[011]//TD$ with a small intensity of 1.4 is formed. For

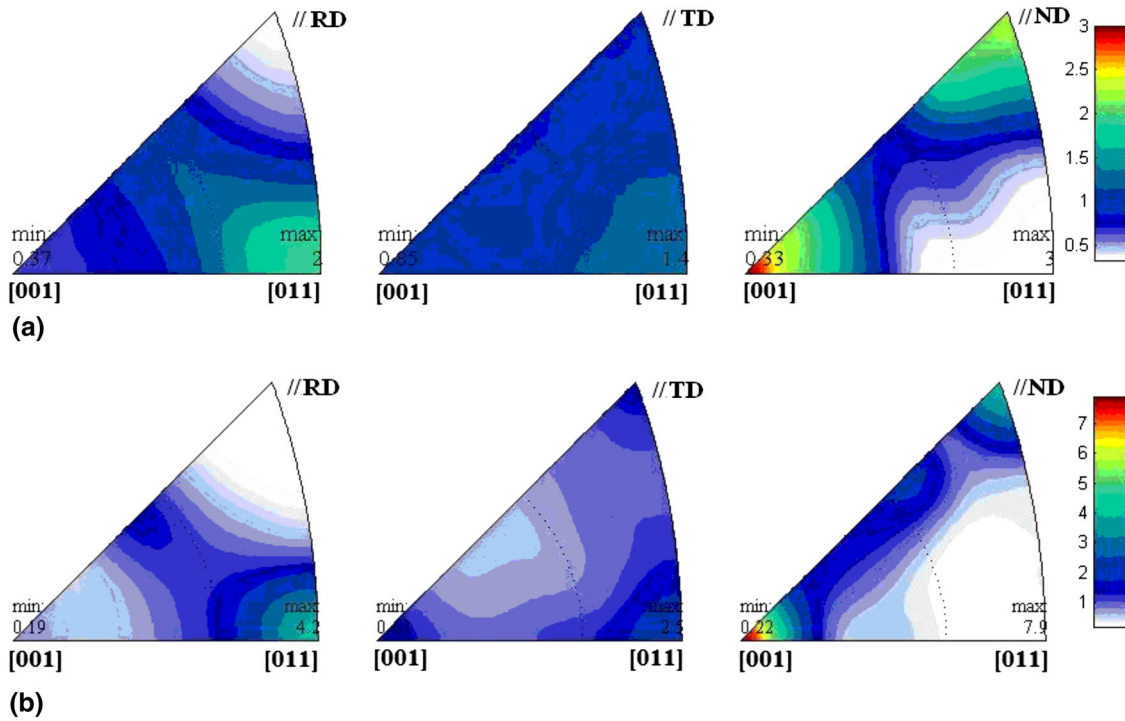


Fig. 14 (110) Inverse pole figure for RD, TD, and ND directions in the case of (a) precursor-2; (b) ARB-8 layers-2

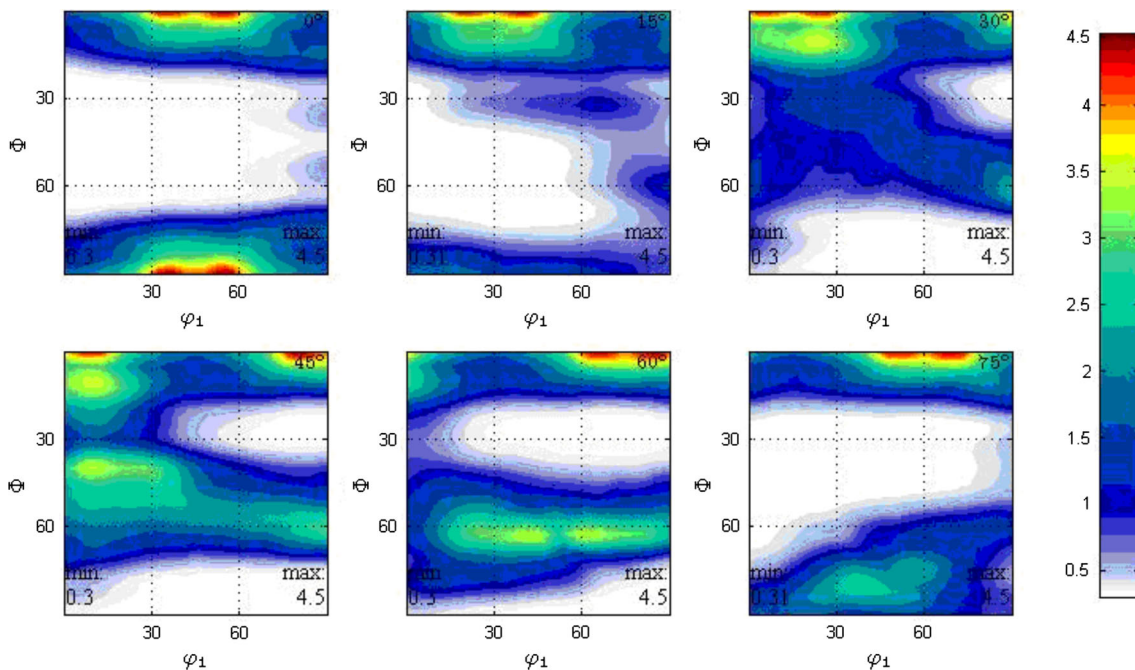


Fig. 15 Orientation distribution function (ODF) for Ti-25Nb-25Ta alloy corresponding to precursor-2 (ODF sections: $\varphi_2 = 0^\circ, 15^\circ, 30^\circ, 45^\circ, 60^\circ,$ and 75°)

the pairs [001]//ND and [011]//ND, the intensities are higher, 3.0 for both pairs. The most capable to develop textures in ARB stage will be the components [001]//ND, [111]//ND, and [011]//RD.

In the case of ARB-8 layers applied on precursor-2 sample (Fig. 14b), there are forming following high intensity pairs: [011]//RD with an intensity of 4.2; [011]//TD with an intensity

of 2.5; and the pair [111]//ND with an intensity of 7.9. If intensities are compared (Fig. 14b, 8b), the conclusion is that the texture intensity is higher for the ARB-8 layers applied on precursor-2 than on ARB-8 layers applied on precursor-1 (7.9 versus 2.5, 2.5 versus 1.7, and 4.2 versus 2.4 for the [011]//ND, [011]//TD, and [011]//RD pairs, respectively).

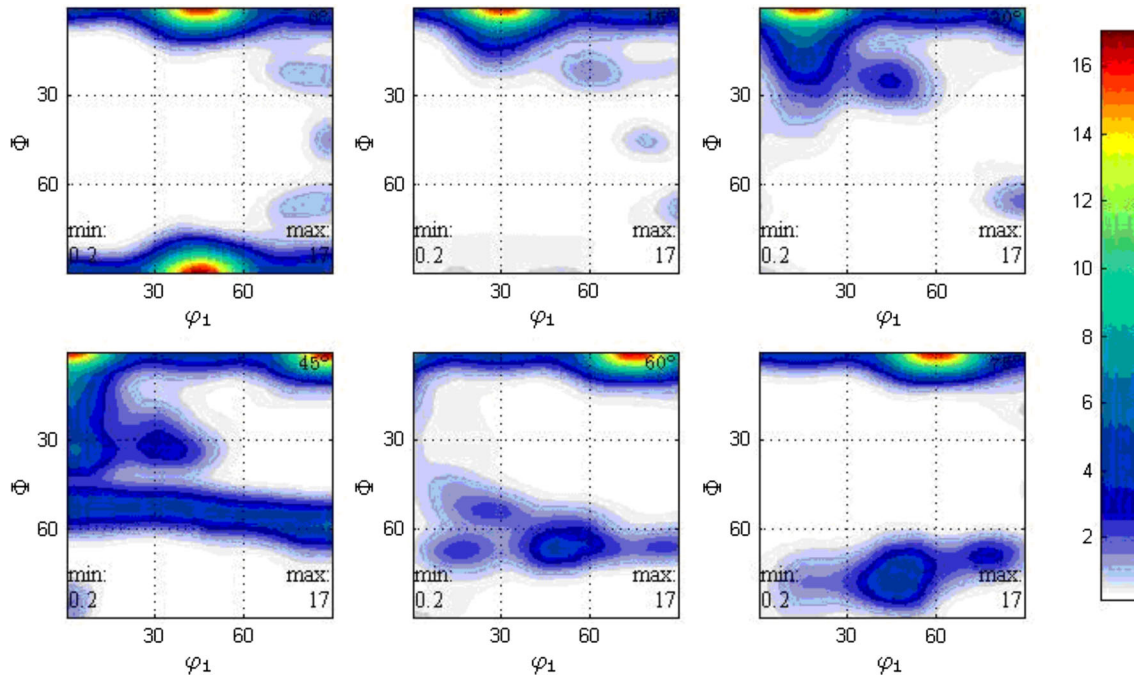


Fig. 16 Orientation distribution function (ODF) for Ti-25Nb-25Ta alloy after ARB-8 layers-2 (ODF sections: $\varphi_2 = 0^\circ, 15^\circ, 30^\circ, 45^\circ, 60^\circ,$ and 75°)

Figure 15 indicates the calculated ODF sections for precursor-2 state. Plotted ODF sections corresponding to $\varphi_2 = 0^\circ$ show the presence of high intensity texture modes $\{001\} \langle 1\bar{1}0 \rangle$ and $\{010\} \langle 101 \rangle$ with a maximum orientation density of 4.5; both texture modes belong to θ -fiber ($\{001\} \langle 110 \rangle$ family) and are formed due to grains shear during cold-rolling deformation.

The ODF section corresponding to $\varphi_2 = 45^\circ$ shows the presence of the following texture modes and fibers:

- high intensity texture modes $\{001\} \langle 1\bar{1}0 \rangle$ and $\{001\} \langle \bar{1}\bar{1}0 \rangle$, showing a maximum orientation density of 4.5; both texture modes belong to θ -fiber ($\{001\} \langle 110 \rangle$ family) and are formed due to grains shear during cold-rolling deformation;
- well-developed γ -fiber: the main component of γ -fiber stretches from $\{111\} \langle 1\bar{1}0 \rangle$ to $\{111\} \langle \bar{1}\bar{1}2 \rangle$; the γ -fiber is the most important developed fiber during TM processing, with a maximum orientation density of 3; and
- well-developed α -fiber: the main component of α -fiber stretches from $\{001\} \langle 1\bar{1}0 \rangle$ to $\{112\} \langle 1\bar{1}0 \rangle$; the orientation density of α -fiber shows a value close to 3.5, bigger than in the case of γ -fiber.

Figure 16 indicates the calculated ODF sections for ARB applied on precursor-2. Plotted ODF section corresponding to $\varphi_2 = 0^\circ$ shows the presence of high intensity texture modes $\{001\} \langle 1\bar{1}0 \rangle$ and $\{010\} \langle 101 \rangle$ with a maximum orientation density of 17.0; both texture modes belong to θ -fiber ($\{001\} \langle 110 \rangle$ family) and are formed due to grains shear during ARB processing.

The ODF section corresponding to $\varphi_2 = 45^\circ$ shows the presence of the following texture modes and fibers:

- high intensity texture modes $\{001\} \langle 1\bar{1}0 \rangle$ and $\{001\} \langle \bar{1}\bar{1}0 \rangle$, showing a maximum orientation density of 16.0; both texture modes belong to θ -fiber ($\{001\} \langle 110 \rangle$ family)

- and are formed due to grains' shear during ARB process;
- well-developed γ -fiber: the main component of γ -fiber stretches from $\{111\} \langle 1\bar{1}0 \rangle$ to $\{111\} \langle \bar{1}\bar{1}2 \rangle$. The γ -fiber is the most important developed fiber during ARB processing, with maximum orientation density close to 2; and
- well-developed α -fiber: the main component of α -fiber stretches from $\{001\} \langle 1\bar{1}0 \rangle$ to $\{112\} \langle 1\bar{1}0 \rangle$. The orientation density of α -fiber shows a value close to 2.5, bigger than in the case of γ -fiber.

From ODF data analysis, corresponding to ARB-processed alloy, it can be concluded that the developed texture during ARB processing shows a strong $\{001\} \langle 110 \rangle$ rolling texture; the main orientation component spreads from $\{001\} \langle 1\bar{1}0 \rangle$ to $\{001\} \langle \bar{1}\bar{1}0 \rangle$; α and γ -fibers are the most well-developed, the α -fiber texture being the most important texture mode.

ARB applied on precursor-2 seems to indicate the highest intensity texture modes, with a maximum orientation density of 17.0, comparative to ARB applied on precursor-1 which indicates a maximum orientation density of 5.6 only.

4. Conclusions

A TM process combined with a SPD/ARB processing route was used to obtain multi-layered stacked strips with NC structure in a Ti-25Nb-25Ta alloy. The ARB method was selected among other SPD possibilities and was identically applied, in three steps, on two types of precursor samples: precursor-1 was cold rolled, recrystallized, and cold rolled again; precursor-2 was cold rolled, recrystallized, cold rolled again, and finally recrystallized. The \bar{B}_0 and \bar{M}_d parameters have been calculated for Ti-25Nb-25Ta alloy in order to find

the alloy position in $\overline{Bo}-\overline{Md}$ diagram and thus to evaluate the main deformation mechanisms possible to act, depending on β phase stability.

The texture intensity is higher for ARB applied on precursor-2, compared with precursor-1 (7.9 versus 2.5, 2.5 versus 1.7, and 4.2 versus 2.4 for the [011]//ND, [011]//TD and [011]//RD pairs, respectively). The highest intensity texture modes have been obtained also for ARB applied on precursor-2, with a maximum orientation density of 17.0, compared to the ARB applied on precursor-1 with a maximum orientation density of 5.6 only.

The alloy microstructure for both precursor samples consists mostly of β -Ti phase with a small amount of α'' -Ti phase grains (6% for precursor-1 and 0.38% for precursor-2, respectively). After ARB process, the structure reveals an increased quantity of α'' -phase, of about 39 to 41.06%.

In the as-studied cases, the applied ARB process leads to an evident stress-induced martensitic transformation, with an increase of α'' phase quantity of about 33 to 40%. The final obtained NC structure underlines the idea that ARB process is useful for structure refining in correlation with β -Ti/ α'' -Ti ratio evolution.

Acknowledgment

This work was supported by a grant of the Romanian National Authority for Scientific Research, CCCDI—UEFISCDI, Project No. MNT-7-075/2013.

References

1. M. Geetha, A.K. Singh, R. Asokamani, and A.K. Gogia, Ti Based Biomaterials, the Ultimate Choice for Orthopaedic Implants—A Review, *Prog. Mater. Sci.*, 2009, **54**, p 397–425
2. M. Abdel-Hady Gepreel and M. Niinomi, Biocompatibility of Ti-Alloys for Long-Term Implantation, *J. Mech. Behav. Biomed. Mater.*, 2013, **20**, p 407–415
3. K.Y. Xie, Y. Wang, Y. Zhao, L. Chang, G. Wang, Z. Chen, Y. Cao, X. Liao, E.J. Lavermia, R.Z. Valiev, B. Sarrafpour, H. Zoellner, and S.P. Ringer, Nanocrystalline β -Ti Alloy with High Hardness, Low Young's Modulus and Excellent In Vitro Biocompatibility for Biomedical Applications, *Mater. Sci. Eng. C*, 2013, **33**(6), p 3530–3536
4. M. Niinomi, M. Nakai, Titanium-Based Biomaterials for Preventing Stress Shielding between Implant Devices and Bone, *Int J Biomater.*, 2011, doi:10.1155/2011/836587
5. Z. Lin, L. Wang, X. Xue, W. Lua, J. Qin, and D. Zhang, Microstructure Evolution and Mechanical Properties of a Ti-35Nb-3Zr-2Ta Biomedical Alloy Processed by Equal Channel Angular Pressing (ECAP), *Mater. Sci. Eng. C*, 2013, **33**, p 4551–4561
6. D. Kent, G. Wang, and M. Dargusch, Effects of Phase Stability and Processing on the Mechanical Properties of Ti-Nb Based β Ti Alloys, *J. Mech. Behav. Biomed. Mater.*, 2013, **28**, p 15–25
7. W. Xu, D.P. Edwards, X. Wu, M. Stoica, M. Calin, U. Kühn, J. Eckert, and K. Xia, Promoting Nano/Ultrafine-Duplex Structure Via Accelerated a Precipitation in a β -Type Titanium Alloy Severely Deformed by High-Pressure Torsion, *Scripta Mater.*, 2013, **68**, p 67–70
8. Y. Wang, J. Zhao, S. Dai, F. Chen, X. Yu, and Y. Zhang, Influence of Cold Rolling and Ageing Treatment on Microstructure and Mechanical Properties of Ti-30Nb-5Ta-6Zr alloy, *J. Mech. Behav. Biomed. Mater.*, 2013, **27**, p 33–42
9. E. Vasilescu, P. Drob, D. Raducanu, V.D. Cojocaru, I. Cinca, D. Iordachescu, R. Ion, M. Popa, and C. Vasilescu, In Vitro Biocompatibility and Corrosion Resistance of a New Implant Titanium Base Alloy, *J. Mater. Sci.*, 2010, **21**, p 1959–1968
10. P. Laheurte, F. Prima, A. Eberhardt, T. Gloriant, M. Wary, and E. Patoor, Mechanical Properties of Low Modulus Beta Titanium Alloys Designed from the Electronic Approach, *J. Mech. Behav. Biomed. Mater.*, 2010, **3**, p 565–573
11. S.J. Li, T.C. Cui, Y.L. Hao, and R. Yang, Fatigue Properties of a Metastable Beta-Type Titanium Alloy with Reversible Phase Transformation, *Acta Biomater.*, 2008, **4**, p 305–317
12. Y. Al-Zain, H.Y. Kim, H. Hosoda, T.H. Nam, and S. Miyazaki, Shape Memory Properties of Ti-Nb-Mo Biomedical Alloys, *Acta Mater.*, 2010, **58**, p 4212–4223
13. H.Y. Kim, Y. Ikehara, J.I. Kim, H. Hosoda, and S. Miyazaki, Martensitic Transformation, Shape Memory Effect and Superelasticity of Ti-Nb Binary Alloys, *Acta Mater.*, 2006, **54**, p 2419–2429
14. S. Yamaguchi, H. Takadama, T. Matsushita, T. Nakamura, and T. Kokubo, Apatite-Forming Ability of Ti-15Zr-4Nb-4Ta Alloy Induced By Calcium Solution Treatment, *J. Mater. Sci.*, 2010, **21**, p 439
15. R.Z. Valiev, Y. Estrin, Z. Horita, T.G. Langdon, M.J. Zehetbauer, and Y.T. Zhu, Producing Bulk Ultrafine-Grained Materials by Severe Plastic Deformation, *JOM*, 2006, **58**, p 33–39
16. K. Cheng, C. Lu, K. Tieu, and H. Zhu, Microstructural Evolution and Mechanical Property of AA5050 Alloy Deformed by Accumulative Roll Bonding, *Metall. Mater. Trans. B*, 2014, **45**(2), p 399–403
17. I. Cinca, D. Raducanu, A. Nocivin, D.M. Gordin, and V.D. Cojocaru, Formation of Nano-Sized Grains in Ti-10Zr-5Nb-5Ta Biomedical Alloy Processed by Accumulative Roll Bonding (ARB), *Kovove Mater.*, 2013, **51**(3), p 165–172
18. D. Terada, S. Inoue, and N. Tsuji, Microstructure and Mechanical Properties of Commercial Purity Ti Severely Deformed by ARB Process, *J. Mater. Sci.*, 2007, **42**(5), p 1673–1681
19. V.D. Cojocaru, D. Raducanu, T. Gloriant, and I. Cinca, Texture Evolution in a Ti-Ta-Nb Alloy Processed by Severe Plastic Deformation, *JOM*, 2012, **64**(5), p 572–581
20. E. Vasilescu, P. Drob, C. Vasilescu, S.I. Drob, E. Bertrand, D.M. Gordin, and T. Gloriant, Corrosion Resistance of the New Ti-25Ta-25Nb Alloy in Severe Functional Conditions, *Mater. Corros.*, 2010, **61**, p 947–954
21. D.M. Gordin, D. Busardo, A. Cimpean, C. Vasilescu, D. Höche, S.I. Drob, V. Mitran, M. Cornen, and T. Gloriant, Design of a Nitrogen-Implanted Titanium-Based Super-Elastic Alloy with Optimized Properties for Biomedical Applications, *Mater. Sci. Eng. C*, 2013, **33**(7), p 4173–4182
22. E. Bertrand, T. Gloriant, D.M. Gordin, E. Vasilescu, P. Drob, C. Vasilescu, and S.I. Drob, Synthesis and Characterisation of a New Super-Elastic Ti-25Ta-25Nb Biomedical Alloy, *J. Mech. Behav. Biomed. Mater.*, 2010, **3**, p 559–564
23. E. Bertrand, P. Castany, and T. Gloriant, Investigation of the Martensitic Transformation and the Damping Behaviour of a Super-Elastic Ti-Ta-Nb Alloy, *Acta Mater.*, 2013, **61**, p 511–518
24. A. Cimpean, V. Mitran, C.M. Ciofrangeanu, B. Galateanu, E. Bertrand, D.M. Gordin, D. Iordachescu, and T. Gloriant, Osteoblast Cell Behavior on the New Beta-Type Ti-25Ta-25Nb Alloy, *Mater. Sci. Eng. C*, 2012, **32**(6), p 1554–1563
25. F. Bachmann, R. Hielscher, and H. Schaeben, Texture Analysis with MTEX—Free and Open Source Software Toolbox, *Solid State Phenom.*, 2010, **160**, p 63–68
26. F. Bachmann, R. Hielscher, P.E. Jupp, W. Pantleon, H. Schaeben, and E. Wegert, Inferential Statistics of Electron Backscatter Diffraction Data from Within Individual Crystalline Grains, *J. Appl. Crystallogr.*, 2010, **43**, p 1338–1355
27. D. Raabe, B. Sander, M. Friak, D. Ma, and J. Neugebauer, Theory-Guided Bottom-Up Design of β -Titanium Alloys as Biomaterials Based on First Principles Calculations: Theory and Experiments, *Acta Mater.*, 2007, **55**, p 4475–4487
28. T. Zhou, M. Aindow, S.P. Alpay, M.J. Blackburn, and M.H. Wu, Pseudo-Elastic Deformation Behaviour in a Ti/Mo-Based Alloy, *Scripta Mater.*, 2004, **50**(3), p 343–348
29. P.J. Bania, Beta Titanium Alloys and Their Role in the Titanium Industry, *J. Met.*, 1994, **41**, p 16–19
30. M. Abdel-Hady, K. Hinoshita, and M. Morinaga, General Approach to Phase Stability and Elastic Properties of β -Type Ti-Alloys Using Electronic Parameters, *Scripta Mater.*, 2006, **55**(5), p 477–480
31. Morinaga, M., Yukawa, N., Maya, T., Sone, K., Adachi, H., Theoretical Design of Titanium Alloys. In: *Proceedings of Sixth World Conference on Titanium*, Cannes, France, 6–9 June 1988, Société Française de Metallurgie, p 1601–1606
32. D.C. Zhang, J.G. Lin, W.J. Jiang, M. Ma, and Z.G. Peng, Shape Memory and Super-Elastic Behaviour of Ti-7.5Nb-4Mo-1Sn Alloy, *Mater. Design*, 2011, **32**, p 4614–4617

33. S. Neelakantan, R. Rivera-Diaz-del-Castillo, and S. van der Zwaag, Prediction of the Martensite Start Temperature for Beta Titanium Alloys as a Function of Composition, *Scripta Mater.*, 2009, **60**, p 611–614
34. J. He, F. Zhou, G. Chang, and E.J. Lavernia, Influence of Mechanical Milling on Microstructure of 49Fe-49Co-2V Soft Magnetic Alloy, *J. Mater. Sci.*, 2001, **36**(12), p 2955–2964
35. H.Y. Kim, T. Sasaki, K. Okutsu, J.I. Kim, T. Inamura, H. Hosada, and S. Myazaki, Texture and Shape Memory Behaviour of Ti-22Nb-6Ta Alloy, *Acta Mater.*, 2006, **54**(2), p 423–433
36. P. Majumdar, S.B. Singh, and M. Chakraborty, Elastic Modulus of Biomedical Titanium Alloys by Nano-Indentation and Ultrasonic Techniques—A Comparative Study, *Mater. Sci. Eng. A*, 2008, **489** (1–2), p 419–425
37. N.P. Gurao, A. Ali, and S. Suwas, Study of Texture Evolution in Metastable β -Ti Alloy as a Function of Strain Path and its Effect on α Transformation Texture, *Mater. Sci. Eng. A*, 2009, **504**(1–2), p 24–35
38. Z. Ahmad and A. ul Haq, Texture, Microstructure and Magnetic Properties of Fe-28Cr-15Co-3.5Mo Permanent Magnet, *J. Magn. Mater.*, 2009, **321**(4), p 325–329
39. B. Sander and D. Raabe, Texture Inhomogeneity in a Ti-Nb-Based β -Titanium Alloy After Warm Rolling and Recrystallization, *Mater. Sci. Eng. A*, 2008, **479**(1–2), p 236–247
40. Y.B. Wang, Y.H. Zhao, Q. Lian, X.Z. Liao, R.Z. Valiev, S.P. Ringer, Y.T. Zhu, and E.J. Lavernia, Grain Size and Reversible Beta-to-Omega Phase Transformation in a Ti Alloy, *Scripta Mater.*, 2010, **63**, p 613–616